

Chemical-Pressure-Modulated BaTiO₃ Thin Films with Large Spontaneous Polarization and High Curie Temperature

Yilin Wang, Linxing Zhang, Jiaou Wang, Qiang Li, Huanhua Wang, Lin Gu, Jun Chen, Jinxia Deng, Kun Lin, Ling Huang, and Xianran Xing*

Cite This: *J. Am. Chem. Soc.* 2021, 143, 6491–6497

Read Online

ACCESS |



Metrics & More

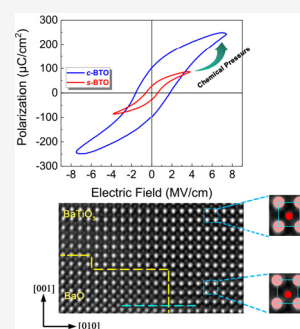


Article Recommendations



Supporting Information

ABSTRACT: Although BaTiO₃ is one of the most famous lead-free piezomaterials, it suffers from small spontaneous and low Curie temperature. Chemical pressure, as a mild way to modulate the structures and properties of materials by element doping, has been utilized to enhance the ferroelectricity of BaTiO₃ but is not efficient enough. Here, we report a promoted chemical pressure route to prepare high-performance BaTiO₃ films, achieving the highest remanent polarization, P_r (100 $\mu\text{C}/\text{cm}^2$), to date and high Curie temperature, T_c (above 1000 $^\circ\text{C}$). The negative chemical pressure (~ -5.7 GPa) was imposed by the coherent lattice strain from large cubic BaO to small tetragonal BaTiO₃, generating high tetragonality ($c/a = 1.12$) and facilitating large displacements of Ti. Such negative pressure is especially significant to the bonding states, i.e., hybridization of Ba 5p–O 2p, whereas ionic bonding in bulk and strong bonding of Ti e_g and O 2p, which contribute to the tremendously enhanced polarization. The promoted chemical pressure method shows general potential in improving ferroelectric and other functional materials.



INTRODUCTION

The strong coupling of the lattice, spin, and orbit under pressure brings diverse properties into solid-state materials, such as superconductivity, multiferroics, ferromagnetism, etc.^{1–3} In the category of the origin, pressure could be divided into external physical pressure and inner chemical pressure. Physical hydrostatic pressure, as an external pressure usually loaded through a diamond anvil cell, is mechanically applied to the material to modify the structure and obtain novel properties. A marvelous example is the discovery of a room-temperature superconductor under extreme pressure of 267 GPa.⁴ Chemical pressure as an internal pressure is another effective way to tailor functional materials. It is generally perceived as an exerted force caused by the lattice strain through heterogeneous substitution in the lattice. In most cases, negative pressure could be obtained by introducing chemical species with large sizes, which is of significance to develop new functionalities. For instance, the negative pressure introduced by doping of Ga³⁺ and Fe³⁺ in the ScF₃ lattice would enlarge the lattice volume and subsequently achieve zero thermal expansion in a wide temperature range,⁵ and rare earth doping could impose tunable negative chemical pressure to RuSr₂(R_{2–x}Ce_x)Cu₂O_{10–δ} to obtain a robust variation of negative magnetoresistance.⁶ Nevertheless, the tolerance of the lattice against substitution is finite, indicating a limited magnitude of chemical pressure by element dopant, such as -0.36 GPa for Sc_{1–x}Fe_xF₃ with 10% Fe³⁺ doping and negative pressure of -0.15 GPa introduced by Fe for TeCo_{1.9}Fe_{0.1}.^{5,7} It is a big challenge but of great value to pursue a path to gain a

large negative pressure and modulate the properties in solid-state matter.

In our previous study, we promoted the chemical route and successfully imposed large negative chemical pressure to PbTiO₃ nanocrystals and their films.^{8,9} Inner coherent interface, through size effect or heterostructural interphase strain imposed by PbO, is introduced to the matrix to achieve remarkably strengthened negative chemical pressure compared to the mild chemical pressure in heterogeneously doped lattice, and negative pressure was demonstrated to be vital for the enhancement of ferroelectricity in PbTiO₃. The ferroelectricity of the nanosized ferroelectrics is perceived to decay due to the failure of the long-range Coulomb force. However, through delicate manipulation, PbTiO₃ nanoparticles with sizes down to 12 nm could possess enhanced ferroelectricity due to the negative pressure introduced by the PbO-terminated surface.⁸ The interphase strain applied through the coherence of PbO and PbTiO₃ yields a giant out-of-plane negative pressure, leading to tremendous remanent polarization and high Curie temperature of the PbTiO₃ thin film.⁹

Compared to PbTiO₃ with large remanent polarization but toxic lead composition, lead-free BaTiO₃ is more preferred in practical applications but suffers from small spontaneous

Received: January 18, 2021

Published: April 26, 2021



polarization ($15\text{--}30\text{ }\mu\text{C}/\text{cm}^2$) and low Curie temperature ($130\text{ }^\circ\text{C}$).^{10–12} It remains a more urgent concern in both technology and science to improve the ferroelectric properties of BaTiO_3 .^{13–15} In this article, we employ the promoted chemical route to prepare coherent $\text{BaTiO}_3\text{:BaO}$ epitaxial films. Considerable negative chemical pressure on tetragonal BaTiO_3 is imposed from the large lattice of cubic BaO , which memorably enhances the ferroelectric properties.

EXPERIMENTAL SECTION

Preparation of Thin Films. The $\text{BaTiO}_3\text{:BaO}$ composite thin film (c-BTO) and single-phase BaTiO_3 thin film (s-BTO) were grown by radio frequency magnetron sputtering with (100)-oriented Nb-doped SrTiO_3 as the single-crystal substrate (Nb:STO).

Lattice Structure Characterization. Room-temperature and high-temperature $\theta\text{--}2\theta$ synchrotron X-ray diffraction (sXRD) and reciprocal space mapping (RSM) measurements were carried out at the diffuse X-ray scattering station of the Beijing Synchrotron Facility (1W1A beamline). The $\theta\text{--}2\theta$ scans of c-BTO and s-BTO were performed to obtain the out-of-plane lattice parameters of the films and substrates. The high-resolution synchrotron-based RSM were measured to show the detailed structure around the (103) plane. A ϕ scan was tested by fixing the diffraction plane of (103) and rotating the ϕ angles to determine the symmetry. Auger electron spectroscopy (AES) (PHI-710, ULVAC-PHI, Japan) with depth analysis was used to determine the component distribution in the out-of-plane direction. The cross-sectional high-angle annular dark-field scanning transmission electron microscopy (HAADF-STEM) images were taken with an atomic-resolution analytical microscope (JEM-ARM 200F).

Electrical Characterization. The atomic force microscopy (AFM) and piezoresponse force microscopy (PFM) experiments were carried out with MFP-3D, Asylum Research, with the contacting mode. The patterned PFM image was written with a dc voltage of $\pm 10\text{ V}$ via a conductive PFM tip. Then the reversed domain patterns were read. The dual frequency resonant-tracking technique (DART) was applied to improve the PFM sensitivity. The ferroelectric hysteresis loops at room and high temperatures were measured by a ferroelectric tester (TF-Analyzer 1000, aixACCT, Germany) with the assistance of the high-voltage accessory, and the frequency of the voltage pulse is 1000 Hz. The positive up/negative down (PUND) measurement was carried out with a TF-Analyzer 2000, with frequency voltage pulse of 100 Hz.

Electronic Structure Characterization. The X-ray absorption spectra (XAS) and X-ray photoelectron spectroscopy (XPS) were collected at the photoelectron spectroscopy station of the Beijing Synchrotron Radiation Facility (4B9B beamline). The photon energy was corrected via the Au standard sample to normalize the spectra of Ti *L*-edge and O *K*-edge.

Detailed experiments are provided in Supporting Information.

RESULTS AND DISCUSSION

Other than lattice matching between tetragonal PbTiO_3 and tetragonal PbO ,⁹ cubic BaO ($Fm\bar{3}m$) with a large lattice ($a = 5.35\text{ }\text{\AA}$) was introduced to modify the tetragonal BaTiO_3 , which is difficult but could provide larger negative pressure to BaTiO_3 . In c-BTO, tetragonal BaTiO_3 (Figure 1a) matches well with “tetragonal-like” BaO with the (110) plane (in-plane) and (001) plane in the out-of-plane orientation ($c_t = 5.35\text{ }\text{\AA}$ and $a_t = 3.94\text{ }\text{\AA}$ (equal to $a_{(110)}/2$), represented in Figure 1c). Along these specific directions, the coherent interface of BaTiO_3 and “tetragonal-like” BaO is built (schematically shown in Figure 1b). The a_t value of BaO is close to that of a_{BTO} and $a_{\text{Nb:STO}}$, which benefits the epitaxial growth of c-BTO, and the large c_t could bring about large negative chemical pressure to the BaTiO_3 matrix. The sXRD patterns

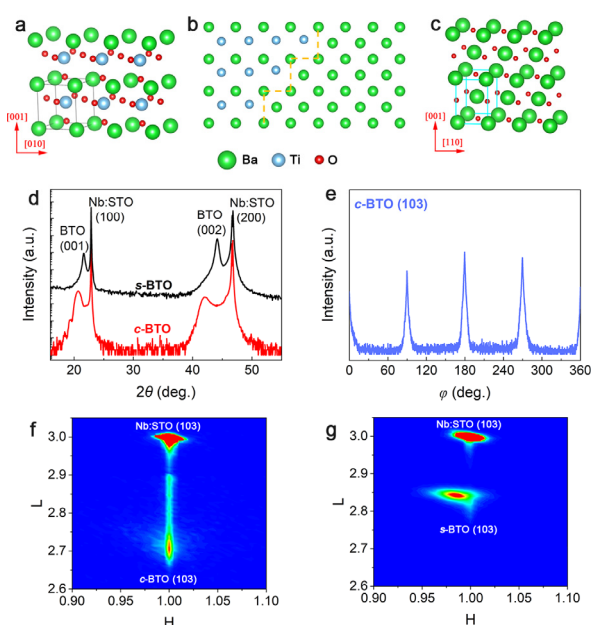


Figure 1. (a,c) Lattice structures of BaTiO_3 and BaO , respectively; (b) interface schematic; (d) sXRD patterns of s-BTO and c-BTO; (e) ϕ scan normal to the (103) plane of c-BTO; (f,g) synchrotron-based RSM about the (103) plane of c-BTO and s-BTO, respectively.

are shown in Figure 1d. As $\theta\text{--}2\theta$ scans could only reveal the out-of-plane orientation, the diffraction patterns of cubic Nb:STO merely include the (100) and (200) planes, whereas tetragonal c-BTO and s-BTO display (001) and (002) planes without other diffraction planes, proving good crystallization and epitaxial growth of c-BTO and s-BTO. Although the c value of s-BTO is determined to be $4.12 \pm 0.003\text{ }\text{\AA}$ from the Bragg diffraction in Figure 1d, which is larger than the bulk counterpart ($c_{\text{BTO}} = 4.034\text{ }\text{\AA}$ and $a_{\text{BTO}} = 3.994\text{ }\text{\AA}$) due to the compressed strain imposed by the Nb:STO substrate, a much enlarged c value of $4.36 \pm 0.003\text{ }\text{\AA}$ is observed in c-BTO, indicating the significance of negative pressure imposed by BaO . The 360° ϕ scan in Figure 1e of c-BTO along the (103) plane shows four-fold rotational symmetry, confirming the tetragonal nature of it even with such enlarged lattice deformation. However, the in-plane parameter of single-crystal substrate Nb:STO and epitaxial thin film is not available in the $\theta\text{--}2\theta$ sXRD patterns. RSM is an efficient tool to determine the detailed crystal structure and lattice parameters of thin films precisely, which has been widely used in epitaxial films.^{16–18} In the RSM of c-BTO around the (103) plane in Figure 1f, the reciprocal space of a part of the HL plane is presented, from which the lattice parameters of both a and c could be derived. The in-plane parameter of c-BTO is coherent with Nb:STO, with $a_{\text{c-BTO}} = 3.91 \pm 0.005\text{ }\text{\AA}$, implying epitaxial growth of c-BTO. The tetragonal distortion ($c/a = 1.12$) is much enhanced due to the negative chemical pressure in c-BTO, which is much larger than the 1.013 of the bulk counterparts or other strained BaTiO_3 thin films.^{19,20} To quantitatively determine the chemical pressure, we proposed the equation counting in the lattice deformation and the elasticity of the lattice:

$$dP = -K \frac{dV}{V_0}$$

where dP is the chemical pressure, K is the bulk modulus, which is 172.6 GPa for BaTiO_3 ,^{21,22} and dV/V_0 is the variation

of the lattice volume. In c-BTO, BaTiO_3 is subjected to negative pressure of -5.7 GPa, which is much larger than the traditional heterogeneous substitution and rather beneficial for the enlarged tetragonality. The bulk modulus of BaO (66.1 GPa) is much smaller, allowing much more deformation when coupling with “hard” BaTiO_3 .²³

Generally, biaxial strain in reduced thickness and defect dipoles have been considered to play important roles in the enhanced c parameters.^{24,25} Moreover, nanocrystals or nanopillars can induce crystal expansion.^{26–31} The thicknesses of s-BTO and c-BTO films are both around 60 nm, which are demonstrated by the X-ray reflectivity measurements and cross-sectional TEM images (see Figure S1). The RSM about the (103) plane proves partial in-plane relaxation of the a parameters of s-BTO, whereas the well-matched a parameter of c-BTO and Nb:STO is observed in the RSM of c-BTO (see Figure 1f,g). Consequently, the biaxial strain has been released in this thickness, and the negative pressure imposed by BaO is considered more essential for the enlarged c parameter. The O 2s XPS spectra show similar oxygen vacancies, and the Ti ions of both c-BTO and s-BTO maintain a quadruple valence detected through the Ti 2p XPS (see Figure S2). This excluded the contribution of defects to the tetragonality.

In c-BTO, BaO is uniformly distributed in the BaTiO_3 matrix, regarded as nanosized substitutional complexes analogous to elemental doping, making the surface and piezoresponse homogeneous, which is very beneficial for its ferroelectric properties, whereas the traditional composite films hardly achieve a smooth and homogeneous texture.^{28,30,31} The depth-dependent AES was employed to detect the composition of c-BTO. The Ar ion sputtering was applied to remove the surface layer. Through increasing the stripping time, the deeper layer would be measured by AES, eventually obtaining the depth-dependent composition. The ratios of Ti and Ba atoms remain nearly constant, revealing the homogeneous component of c-BTO (see Figure 2a). The AFM scan demonstrates

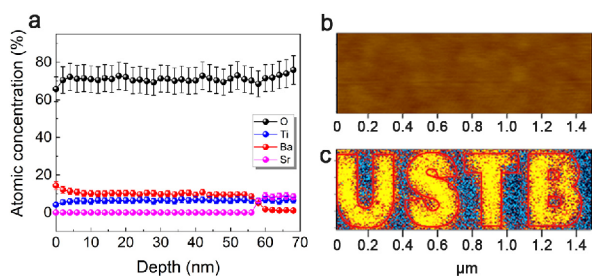


Figure 2. (a) Depth-dependent AES of c-BTO; (b) morphology image, and (c) out-of-plane phase image patterned “USTB” of c-BTO.

the smooth surface with no indication of crystal grain boundaries nor the massive clusters (see Figure S3). The PFM image was patterned with “USTB” by negative and positive poling. Figure 2c unambiguously displays the switched domain image without any obvious nonreversible clusters, further indicating that the distribution of the ferroelectric BaTiO_3 in c-BTO is uniform even in micron order. Meanwhile, the unstained surface in Figure 2b after reverse polarization implicates that the polarization switch of BaTiO_3 does not break the coupling between BaTiO_3 and nonpolar BaO, proving the highly stable coherence.

As the negative pressure imposed by BaO is demonstrated to be vital to enlarge the tetragonality of BaTiO_3 and the coupling

between BaO and BaTiO_3 is homogeneous and stable, the negative pressure is supposed to be able to maintain the ferroelectric phase against increasing temperature due to the elastic interaction. The temperature-dependent evolution of the c value could elucidate the phase transition of a perovskite epitaxial film. Normally, upon heating, the c value of tetragonal BaTiO_3 tends to decrease and turns into an increasing tendency when the phase transition occurs, where the kink is the characteristic of the Curie temperature.^{24,25,30} The c value of c-BTO keeps decreasing without a kink point even at 1000 °C, revealing the tremendously enhanced Curie temperature, which is much higher than that of bulk BaTiO_3 (130 °C) and competitive with the strained ultrathin BaTiO_3 films (Figure S4a,b).^{32,33} The RSMs at 600 and 1000 °C (Figure S5a,b) demonstrate that, although with slight relaxation of the in-plane parameter, c-BTO still possesses the tetragonal structure, confirming the Curie temperature higher than 1000 °C. The ferroelectric nature is still profound at 250 °C, proving a much increased Curie temperature (Figure S6).

The ferroelectric polarization versus electric field hysteresis loop (P – E loop) of c-BTO is measured to show the highest remanent polarization P_r up to 100 $\mu\text{C}/\text{cm}^2$, which is extremely large in BaTiO_3 , whereas the P_r values of s-BTO and BaTiO_3 ceramics are 30 and 15 $\mu\text{C}/\text{cm}^2$, respectively (see Figure 3a and the inset). The hysteresis loops are reproducible,

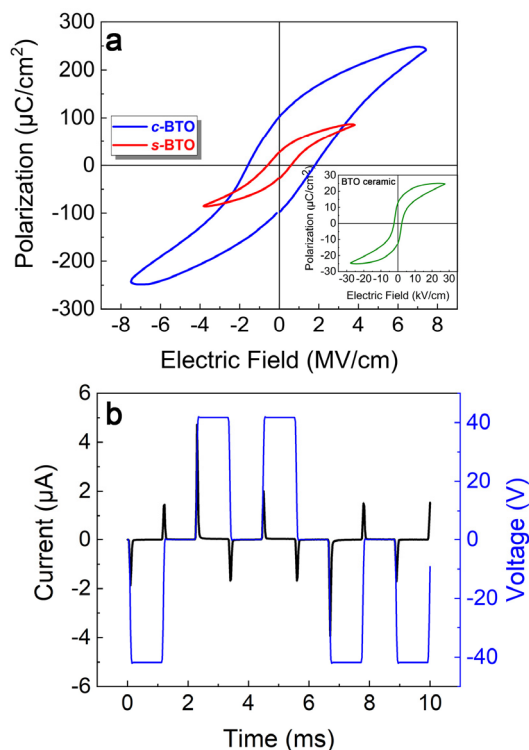


Figure 3. (a) Ferroelectric polarization versus electric field hysteresis loops of c-BTO and s-BTO, with BaTiO_3 ceramics inserted. (b) Positive up/negative down measurement of c-BTO.

as shown in Figure S7. Moreover, the PUND measurement is carried out, with the applied voltage (blue) and detected current (black) shown in Figure 3b. The first pulse is for prepolarizing. The first read pulse is a positive switching pulse, and the second is an unswitched pulse. Likewise, the third and fourth are the negative switching and unswitched pulses, respectively. With the formula

$$\int I dt / A$$

where I is the current, t is the real time, and A is the area of the electrode pad, the saturated polarization could be calculated.³⁴ Here, we get a larger P_s value of $122 \mu\text{C}/\text{cm}^2$ from the PUND measurement than we do from the P_r value of the hysteresis loop. This is because the hysteresis loop of c-BTO is similar to the ferroelectrics designed for energy storage, with large saturated polarization (P_s) and relatively small remanent polarization (P_r). The nonsquare hysteresis behavior is not rare in a composite film, which can be explained by the pinning of the ferroelectric/ferroelastic domain walls by BaO.³⁰ The local phase hysteresis loop of c-BTO film has a fully 180° rotation, and the piezoresponse switching characteristic is classic butterfly-like, confirming the excellent ferroelectric and piezoelectric responses (Figure S8) even at the microscale.

The chemical-pressure-enhanced polarization is meaningful, as strained BaTiO_3 thin films usually do not show obvious enhanced polarization.^{24,25,35} There would be more profound factors other than elastic-interaction-induced elongation. To get a comprehensive understanding of polarization, the atom-level study of c-BTO was performed by cross-sectional HAADF-STEM, where bright spots stand for Ba atoms ($Z = 56$) and the faint spots represent Ti atoms ($Z = 22$), owing to the Z -dependent contrast (see Figure 4a).³⁶ In the STEM

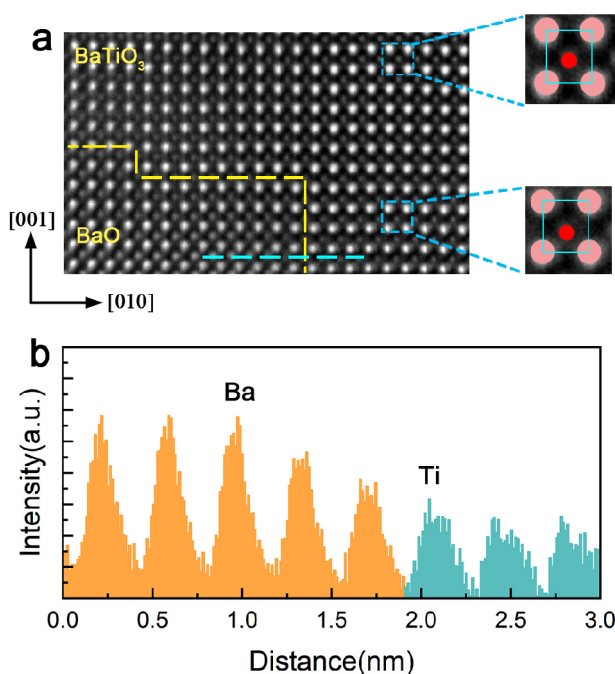


Figure 4. (a) Cross-sectional STEM image of c-BTO, with two BaTiO_3 unit cells magnified in right panels. (b) Intensity profile along the cyan line in (a).

image, two regions with same lattice parameters but different “B”-site brightness are clarified, which could be revealed by the intensity profile along the dashed cyan line exhibited in Figure 4b. The region with bright “B” could be regarded as BaO, and the region with relatively faint “B” is BaTiO_3 , clearly evidencing the coherent interface and lattice match. The displacement of Ti with respect to the center of the surrounding Ba framework (δ_{Ti}) could reflect the magnitude of polarization. It is observed in Figure 4a that δ_{Ti} is reinforced

in BaTiO_3 adjacent to the interface, whereas the far-away unit cell possesses relatively small δ_{Ti} . Two examples of BaTiO_3 unit cells, one close to and another relatively far from the interface, are presented in the magnified panels, with obvious enhanced displacement adjacent to the interface ($\delta_{\text{Ti}} = 0.41 \text{ \AA}$) compared to that of the far-away one ($\delta_{\text{Ti}} = 0.26 \text{ \AA}$). It is worthy to mention that the displacement in bulk BaTiO_3 is only 0.05 \AA , and a polarization of $100 \mu\text{C}/\text{cm}^2$ is expected in BaTiO_3 with $\delta_{\text{Ti}} > 0.2 \text{ \AA}$.³⁷ It is convincing that the negative pressure imposed by BaO could facilitate the displacement of Ti in c-BTO, which is extremely important to the enhanced polarization of BaTiO_3 . To better visualize the enhanced polarization, the displacements are represented by arrays in Figure S9.^{38–40}

It is widely recognized that the hybridization between the oxygen 2p and the titanium 3d states is vital for ferroelectricity of BaTiO_3 and PbTiO_3 .^{41,42} As the ferroelectric polarization of c-BTO is tremendously enhanced, the electronic structures of the films should play a critical role. According to crystal field theory, the 3d orbital is split into high-energy e_g and low-energy t_{2g} in the symmetric octahedron, as shown in Figure 5a. Due to the Jahn–Teller effect when the octahedron is distorted, the doublet e_g is further split into $d_{x^2-y^2}$ and $d_{3z^2-r^2}$, with $d_{3z^2-r^2}$ pointing to the vertex oxygen of the octahedron. The triplet t_{2g} has three orbitals: d_{xy} , d_{yz} , and d_{zx} . When the

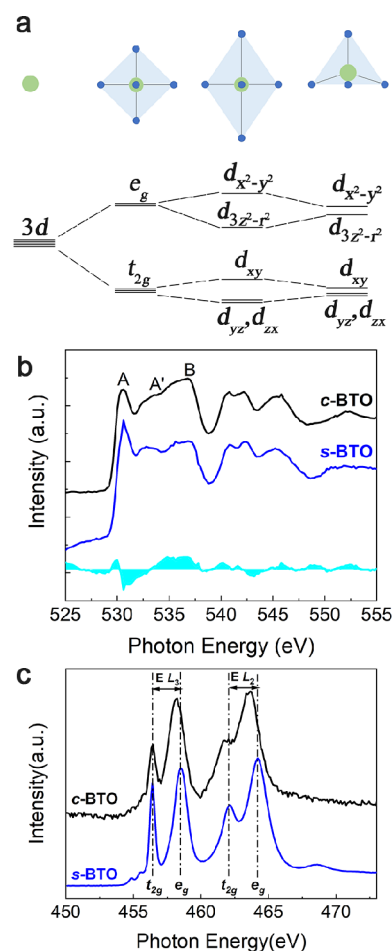


Figure 5. (a) Schematic of the split of the 3d orbital of Ti in the TiO_6 octahedron and TiO_5 pyramid; (b) O K-edge XAS of c-BTO and s-BTO, with the outlined area by subtracting the intensity of s-BTO from that of c-BTO; (c) Ti L-edge XAS of c-BTO and s-BTO.

cation shift is intensified, the oxygen pyramid structure would be generated, with similar energy level of $d_{x^2-y^2}$ and $d_{3z^2-r^2}$.⁴³ To evaluate the electronic structures of c-BTO and s-BTO, O K-edge and Ti L-edge XAS were measured. O K-edge XAS in Figure 5b shows the O 2p partial density, where the A and A' peaks are separately corresponding to the bonding state of Ti t_{2g} and e_g with O 2p, and B peaks reflect the bonding state of Ba 5p and O 2p.⁴⁴ If Ti in c-BTO is placed in the center of the distorted octahedron, the hybridization of $d_{3z^2-r^2}$ and O 2p is weakened due to the elongated distance of titanium and vertex oxygen, making the intensity of the A' peak suppressed. In c-BTO, nevertheless, the A' peak intensity is consistent with s-BTO, which suggests that Ti displacement in the oxygen polyhedron is increased, leading to a nearly unchanged Ti-vertex O distance and uncompromised Ti e_g -O 2p hybridization compared to s-BTO, favoring the oxygen pyramid structure. Two regions of L_3 ($2p_{3/2}$) and L_2 ($2p_{1/2}$) are displayed in the Ti L-edge XAS (Figure 5c). Each of them is split by a crystal field into e_g and t_{2g} . The e_g orbital would further split due to the energy level separation of $d_{x^2-y^2}$ and $d_{3z^2-r^2}$. In a distorted polyhedral crystal field, as shown in Figure 4a, the split of $d_{x^2-y^2}$ and $d_{3z^2-r^2}$ should be enlarged in the elongated c-BTO, while in the actual c-BTO, the split is similar to s-BTO, further proving that in c-BTO the crystal field is more in accord with the pyramid. Moreover, the obvious suppression of the splitting energy of e_g and t_{2g} is due to the larger c/a of c-BTO.⁴⁵ With the Ti atom deviating from the ab plane of the oxygen polyhedron, the Ti d_{xy} -O 2p hybridization would be weakened, which is observed in the suppressed A peak in Figure 5b. The XAS results reveal the enhanced displacement of Ti in the oxygen polyhedron, which tend to form the oxygen pyramid structure. Moreover, the enhanced B peak of c-BTO in Figure 4b is partially due to the transition from an ionic to a covalent bond with a larger c value, which is predicted in BaTiO₃, with the c value exceeding 4.3 Å.⁴⁶ The highly elongated lattice, enhanced Ti displacement, and strong hybridization state of Ti and Ba with O contribute crucially to the polarization.

CONCLUSIONS

In summary, large negative chemical pressure was introduced in the BaTiO₃ composite film by BaO to modulate the structure and ferroelectric properties. Enlarged tetragonality with high Curie temperature (above 1000 °C) and P_r ($\sim 100 \mu\text{C}/\text{cm}^2$) was achieved in this classic lead-free material through the promoted chemical pressure route. Facilitated displacement of Ti, strong bonding states of Ti e_g -O 2p and Ba 5p-O 2p contribute to the tremendous polarization, which is hardly achieved by physical strain engineering in BaTiO₃-based materials. The promoted chemical pressure is expected to be of great inspiration to design many other multifunctional materials.

ASSOCIATED CONTENT

Supporting Information

The Supporting Information is available free of charge at <https://pubs.acs.org/doi/10.1021/jacs.1c00605>.

Experimental details and supporting figures (PDF)

AUTHOR INFORMATION

Corresponding Author

Xianran Xing – Beijing Advanced Innovation Center for Materials Genome Engineering, Institute of Solid State Chemistry, University of Science and Technology Beijing, Beijing 100083, China; orcid.org/0000-0003-0704-8886; Email: xing@ustb.edu.cn

Authors

Yilin Wang – Beijing Advanced Innovation Center for Materials Genome Engineering, Institute of Solid State Chemistry, University of Science and Technology Beijing, Beijing 100083, China; Institute of Advanced Materials (IAM), Jiangsu National Synergetic Innovation Center for Advanced Materials (SICAM), Nanjing Tech University, Nanjing 211816, China

Linxiang Zhang – Beijing Advanced Innovation Center for Materials Genome Engineering, Institute of Solid State Chemistry, University of Science and Technology Beijing, Beijing 100083, China; orcid.org/0000-0002-6767-2771

Jiaou Wang – Institute of High Energy Physics, Chinese Academy of Sciences, Beijing 100049, China

Qiang Li – Beijing Advanced Innovation Center for Materials Genome Engineering, Institute of Solid State Chemistry, University of Science and Technology Beijing, Beijing 100083, China

Huanhua Wang – Institute of High Energy Physics, Chinese Academy of Sciences, Beijing 100049, China

Lin Gu – Beijing National Laboratory for Condensed Matter Physics, Institute of Physics, Chinese Academy of Sciences, Beijing 100190, China; orcid.org/0000-0002-7504-031X

Jun Chen – Beijing Advanced Innovation Center for Materials Genome Engineering, Institute of Solid State Chemistry, University of Science and Technology Beijing, Beijing 100083, China; orcid.org/0000-0002-7330-8976

Jinxia Deng – Beijing Advanced Innovation Center for Materials Genome Engineering, Institute of Solid State Chemistry, University of Science and Technology Beijing, Beijing 100083, China

Kun Lin – Beijing Advanced Innovation Center for Materials Genome Engineering, Institute of Solid State Chemistry, University of Science and Technology Beijing, Beijing 100083, China; orcid.org/0000-0003-4515-3206

Ling Huang – Institute of Advanced Materials (IAM), Jiangsu National Synergetic Innovation Center for Advanced Materials (SICAM), Nanjing Tech University, Nanjing 211816, China; orcid.org/0000-0003-1244-3522

Complete contact information is available at: <https://pubs.acs.org/doi/10.1021/jacs.1c00605>

Notes

The authors declare no competing financial interest.

ACKNOWLEDGMENTS

This research was supported by National Natural Science Foundation of China (22090042 and 21731001) and National Key R&D Program of China (2020YFA0406200). The authors want to thank Qinghua Zhang, Yiru Ji, and Fanqi Meng of the Institute of Physics, Chinese Academy of Sciences, for the STEM measurements, and Zengyao Ren for the preparation of

electrodes by photolithography at the University of Science and Technology Beijing.

REFERENCES

- (1) Somayazulu, M.; Ahart, M.; Mishra, A. K.; Geballe, Z. M.; Baldini, M.; Meng, Y.; Struzhkin, V. V.; Hemley, R. J. Evidence for superconductivity above 260 K in lanthanum superhydride at megabar pressures. *Phys. Rev. Lett.* **2019**, *122*, 027001.
- (2) Aoyama, T.; Yamauchi, K.; Iyama, A.; Picozzi, S.; Shimizu, K.; Kimura, T. Giant spin-driven ferroelectric polarization in TbMnO_3 under high pressure. *Nat. Commun.* **2014**, *5*, 4927.
- (3) Csontos, M.; Mihaly, G.; Janko, B.; Wojtowicz, T.; Liu, X.; Furdyna, J. K. Pressure-induced ferromagnetism in (In, Mn)Sb dilute magnetic semiconductor. *Nat. Mater.* **2005**, *4*, 447.
- (4) Snider, E.; Dasenbrock-Gammon, N.; McBride, R.; Debessai, M.; Vindana, H.; Vencatasamy, K.; Lawler, K. V.; Salamat, A.; Dias, R. P. Room-temperature superconductivity in a carbonaceous sulfur hydride. *Nature* **2020**, *586*, 373.
- (5) Hu, L.; Chen, J.; Fan, L.; Ren, Y.; Rong, Y.; Pan, Z.; Deng, J.; Yu, R.; Xing, X. Zero thermal expansion and ferromagnetism in cubic $\text{Sc}_{1-x}\text{M}_x\text{F}_3$ ($\text{M} = \text{Ga}, \text{Fe}$) over a wide temperature range. *J. Am. Chem. Soc.* **2014**, *136*, 13566.
- (6) McLaughlin, A. C.; Begg, L.; Harrow, C.; Kimber, S. A. J.; Sher, F.; Attfield, J. P. Chemical tuning of positive and negative magnetoresistances, and superconductivity in 1222-type Ruthenocuprates. *J. Am. Chem. Soc.* **2006**, *128*, 12364.
- (7) Song, Y.; Chen, J.; Liu, X.; Wang, C.; Zhang, J.; Liu, H.; Zhu, H.; Hu, L.; Lin, K.; Zhang, S.; Xing, X. Zero thermal expansion in magnetic and metallic $\text{Tb}(\text{Co}, \text{Fe})_2$ intermetallic compounds. *J. Am. Chem. Soc.* **2018**, *140*, 602.
- (8) Sun, J.; Li, Q.; Zhu, H.; Liu, Z.; Lin, K.; Wang, N.; Zhang, Q.; Gu, L.; Deng, J.; Chen, J.; Xing, X. Negative-pressure-induced large polarization in nanosized PbTiO_3 . *Adv. Mater.* **2020**, *32*, 2002968.
- (9) Zhang, L.; Chen, J.; Fan, L. Giant polarization in super-tetragonal thin films through interphase strain. *Science* **2018**, *361*, 494.
- (10) Auciello, O.; Scott, J. F.; Ramesh, R. The physics of ferroelectric memories. *Phys. Today* **1998**, *51*, 22.
- (11) Martin, L.; Rappe, A. Thin-film ferroelectric materials and their applications. *Nat. Rev. Mater.* **2017**, *2*, 16087.
- (12) Ramesh, R. *Thin Film Ferroelectric Materials and Devices*; Springer Science & Business Media: Berlin, 2013.
- (13) Scott, J. F.; Paz de Araujo, C. A. Ferroelectric memories. *Science* **1989**, *246*, 1400.
- (14) Eltes, F.; Caimi, D.; Fallegger, F.; Sousa, M.; O'Connor, E.; Rossell, M. D.; Offrein, B.; Fompeyrine, J.; Abel, S. Low-loss BaTiO_3 -Si waveguides for nonlinear integrated photonics. *ACS Photonics* **2016**, *3*, 1698.
- (15) Murali, P. Ferroelectric thin films for micro-sensors and actuators: a review. *J. Micromech. Microeng.* **2000**, *10*, 136.
- (16) Fewster, P. F. Reciprocal space mapping. *Crit. Rev. Solid State Mater. Sci.* **1997**, *22*, 69.
- (17) Suzuki, H.; Sasaki, T.; Sai, A.; Ohshita, Y.; Kamiya, I.; Yamaguchi, M.; Takahashi, M.; Fujikawa, S. Real-time observation of anisotropic strain relaxation by three-dimensional reciprocal space mapping during InGaAs/GaAs (001) growth. *Appl. Phys. Lett.* **2010**, *97*, 041906.
- (18) Saito, K.; Ulyanenko, A.; Grossmann, V.; Röss, H.; Brueggemann, L.; Ohta, H.; Kurosawa, T.; Ueki, S.; Funakubo, H. Structural characterization of BiFeO_3 thin films by reciprocal space mapping. *Jpn. J. Appl. Phys.* **2006**, *45*, 7311.
- (19) Yanase, N.; Abe, K.; Fukushima, N.; Kawakubo, T. Thickness dependence of ferroelectricity in heteroepitaxial BaTiO_3 thin film capacitors. *Jpn. J. Appl. Phys.* **1999**, *38*, S305.
- (20) Sinsheimer, J.; Callori, S. J.; Ziegler, B.; Bein, B.; Chinta, P. V.; Ashrafi, A.; Headrick, R. L.; Dawber, M. In-situ X-ray diffraction study of the growth of highly strained epitaxial BaTiO_3 thin films. *Appl. Phys. Lett.* **2013**, *103*, 242904.
- (21) Berlincourt, D.; Jaffe, H. Elastic and piezoelectric coefficients of single-crystal Barium Titanate. *Phys. Rev.* **1958**, *111*, 143.
- (22) Schneider, G. A.; Heyer, V. Influence of the electric field on Vickers indentation crack growth in BaTiO_3 . *J. Eur. Ceram. Soc.* **1999**, *19*, 1299.
- (23) Zhuravlev, Y. N.; Korabel'nikov, D. V. Elastic and photoelastic properties of $\text{M}(\text{NO}_3)_2$, MO ($\text{M} = \text{Mg}, \text{Ca}, \text{Sr}, \text{Ba}$). *Russ. Phys. J.* **2017**, *60*, 149.
- (24) Damodaran, A. R.; Breckenfeld, E.; Chen, Z.; Lee, S.; Martin, L. W. Enhancement of ferroelectric Curie temperature in BaTiO_3 films via strain-induced defect dipole alignment. *Adv. Mater.* **2014**, *26*, 6341.
- (25) Choi, K. J.; Biegalski, M.; Li, Y. L. Enhancement of ferroelectricity in strained BaTiO_3 thin films. *Science* **2004**, *306*, 1005.
- (26) Tsunekawa, S.; Ishikawa, K.; Li, Z.-Q.; Kawazoe, Y.; Kasuya, A. Erratum: Origin of anomalous lattice expansion in oxide nanoparticles. *Phys. Rev. Lett.* **2002**, *89*, 249905.
- (27) Hailstone, R. K.; DiFrancesco, A. G.; Leong, J. G.; Allston, T. D.; Reed, K. J. A study of lattice expansion in CeO_2 nanoparticles by transmission electron microscopy. *J. Phys. Chem. C* **2009**, *113*, 15155.
- (28) MacManus-Driscoll, J. L. Self-assembled heteroepitaxial oxide nanocomposite thin film structures: designing interface-induced functionality in electronic materials. *Adv. Funct. Mater.* **2010**, *20*, 2035.
- (29) Lu, L.; Li, L.; Wang, X.; Li, G. Understanding of the finite size effects on lattice vibrations and electronic transitions of nano $\alpha\text{-Fe}_2\text{O}_3$. *J. Phys. Chem. B* **2005**, *109*, 17151.
- (30) Harrington, S. A.; Zhai, J.; Denev, S.; Gopalan, V.; Wang, H.; Bi, Z.; Redfern, S. A. T.; Baek, S.-H.; Bark, C. W.; Eom, C.-B.; Jia, Q.; Vickers, M. E.; MacManus-Driscoll, J. L. Thick lead-free ferroelectric films with high Curie temperatures through nanocomposite-induced strain. *Nat. Nanotechnol.* **2011**, *6*, 491.
- (31) Zheng, H.; Wang, J.; Lofland, S. E. Multiferroic $\text{BaTiO}_3\text{-CoFe}_2\text{O}_4$ nanostructures. *Science* **2004**, *303*, 661.
- (32) Comes, R.; Lambert, M.; Guinier, A. The chain structure of BaTiO_3 and KNbO_3 . *Solid State Commun.* **1968**, *6*, 715.
- (33) Tenne, D. A.; Turner, P.; Schmidt, J. D.; Biegalski, M.; Li, Y. L.; Chen, L. Q.; Soukiassian, A.; Trolier-McKinstry, S.; Schlom, D. G.; Xi, X. X.; Fong, D. D.; Fuoss, P. H.; Eastman, J. A.; Stephenson, G. B.; Thompson, C.; Streiffer, S. K. Ferroelectricity in Ultrathin BaTiO_3 Films: Probing the Size Effect by Ultraviolet Raman Spectroscopy. *Phys. Rev. Lett.* **2009**, *103*, 177601.
- (34) Wei, Y.; Nukala, P.; Salverda, M.; Matzen, S.; Zhao, H. J.; Momand, J.; Everhardt, A. S.; Agnus, G.; Blake, G. R.; Lecoeur, P.; Kooi, B. J.; Iniguez, J.; Dkhil, B.; Noheda, B. A rhombohedral ferroelectric phase in epitaxially strained $\text{Hf}_0.5\text{Zr}_0.5\text{O}_2$ thin films. *Nat. Mater.* **2018**, *17*, 1095.
- (35) Lin, J. L.; He, R.; Lu, Z.; Lu, Y.; Wang, Z.; Zhong, Z.; Zhao, X.; Li, R.-W.; Zhang, Z. D.; Wang, Z. J. Oxygen vacancy enhanced ferroelectricity in BTO:SRO nanocomposite films. *Acta Mater.* **2020**, *199*, 9.
- (36) Catalan, G.; Lubk, A.; Vlooswijk, A. H. G.; Snoeck, E.; Magen, C.; Janssens, A.; Rispens, G.; Rijnders, G.; Blank, D. H. A.; Noheda, B. Ferroelectric rotation of polarization in ferroelectric thin films. *Nat. Mater.* **2011**, *10*, 963.
- (37) Kim, S.-D.; Hwang, G.-T.; Song, K.; Jeong, C. K.; Park, K.-I.; Jang, J.; Kim, K.-H.; Ryu, J.; Choi, S.-Y. Inverse size-dependence of piezoelectricity in single BaTiO_3 nanoparticles. *Nano Energy* **2019**, *58*, 78.
- (38) Tang, Y. L.; Zhu, Y. L.; Ma, X. L.; Borisevich, A. Y.; Morozovska, A. N.; Eliseev, E. A.; Wang, W. Y.; Wang, Y. J.; Xu, Y. B.; Zhang, Z. D.; Pinnycok, S. J. Observation of a periodic array of flux-closure quadrants in strained ferroelectric PbTiO_3 films. *Science* **2015**, *348*, 547.
- (39) Tang, Y. L.; Zhu, Y. L.; Liu, Y.; Wang, Y. J.; Ma, X. L. Giant linear strain gradient with extremely low elastic energy in a perovskite nanostructure array. *Nat. Commun.* **2017**, *8*, 15994.
- (40) Wang, Y. J.; Feng, Y. P.; Zhu, Y. L.; Tang, Y. L.; Yang, L. X.; Zou, M. J.; Geng, W. R.; Han, M. J.; Guo, X. W.; Wu, B.; Ma, X. L. Polar Meron lattice in strained oxide ferroelectrics. *Nat. Mater.* **2020**, *19*, 881.

(41) Cohen, R. E. Origin of ferroelectricity in perovskite oxides. *Nature* **1992**, 358, 136.

(42) Yashima, M.; Omoto, K.; Chen, J.; Kato, H.; Xing, X. Evidence for (Bi,Pb)-O Covalency in the High T_C Ferroelectric PbTiO_3 - BiFeO_3 with Large Tetragonality. *Chem. Mater.* **2011**, 23, 3135.

(43) Ko, K.-T.; Jung, M. H.; He, Q.; Lee, J. H.; Woo, C. S.; Chu, K.; Seidel, J.; Jeon, B.-G.; Oh, Y. S.; Kim, K. H.; Liang, W.-I.; Chen, H.-J.; Chu, Y.-H.; Jeong, Y. H.; Ramesh, R.; Park, J.-H.; Yang, C.-H. Concurrent transition of ferroelectric and magnetic ordering near room temperature. *Nat. Commun.* **2011**, 2, 567.

(44) Chasse, A.; Borek, S.; Schindler, K.-M.; Trautmann, M.; Huth, M.; Steudel, F.; Makhova, L.; Grafe, J.; Denecke, R. High-resolution x-ray absorption spectroscopy of BaTiO_3 : Experiment and first-principles calculations. *Phys. Rev. B: Condens. Matter Mater. Phys.* **2011**, 84, 195135.

(45) Zhao, H.; Miao, J.; Zhang, L.; Rong, Y.; Chen, J.; Deng, J.; Yu, R.; Cao, J.; Wang, H.; Xing, X. Lattice distortion and orbital hybridization in NdFeO_3 - PbTiO_3 ferroelectric thin films. *Dalton. T.* **2016**, 45, 1554.

(46) Shi, J.; Grinberg, I.; Wang, X.; Rappe, A. M. Atomic sublattice decomposition of piezoelectric response in tetragonal PbTiO_3 , BaTiO_3 , and KNbO_3 . *Phys. Rev. B: Condens. Matter Mater. Phys.* **2014**, 89, 094105.